A Landscape of Mesoscale Eddy Vertical Structure: The Influence of Bathymetric Slope and Roughness on Kinetic Energy

JACOB M. STEINBERG,[a,b] ELIZABETH YANKOVSKY,[c,d] SYLVIA T. COLE,[b] AND LAURE ZANNA[c]

[a] *NOAA/Geophysical Fluid Dynamics Laboratory, Princeton, New Jersey*
[b] *Department of Physical Oceanography, Woods Hole Oceanographic Institution, Woods Hole, Massachusetts*
[c] *Courant Institute of Mathematical Sciences and Center for Data Science, New York University, New York, New York*
[d] *Department of Earth and Planetary Sciences, Yale University, New Haven, Connecticut*

(Manuscript received 20 February 2025, in final form 17 June 2025, accepted 23 July 2025)

ABSTRACT: Surface and upper-ocean measurements of mesoscale eddies have revealed the central role they play in ocean transport, but their interior and deep ocean characteristics remain undersampled and underexplored. In this study, mooring arrays, sampling with high vertical resolution, and a high-resolution global atmosphere–ocean coupled simulation are used to characterize full-depth mesoscale eddy vertical structure. The vertical structure of eddy kinetic energy, e.g., partitioning of barotropic to baroclinic eddy kinetic energy or vertical modal structure, is shown to depend partly on bathymetric slope and roughness. This influence is contextualized alongside additional factors, such as latitude and vertical density stratification, to present a global landscape of vertical structure. The results generally reveal eddy vertical structure to decay with increasing depth, consistent with theoretical expectations relating to the roles of surface-intensified stratification and buoyancy anomalies. However, at high latitudes and where the seafloor is markedly flat and smooth (approximately 20% of the ocean's area), mesoscale eddy vertical structures are significantly more barotropic by an approximate factor of 2–5. From a climate modeling perspective, these results can inform the construction, implementation, and improvement of energetic parameterizations that account for the underrepresentation of mesoscale eddies and their effects. They also offer expectation as to a landscape of eddy vertical structure to be used in inferring vertical structure from surface measurements.

SIGNIFICANCE STATEMENT: This work addresses the question of how do ocean seafloor features (bathymetry) affect the vertical structure of ocean currents and eddies? Seafloor features modify eddies in complex ways not often accounted for in global ocean simulations. We analyze high-resolution velocity observations, find diverse structures at four mooring sites, and consider how sloping and rough bathymetry change distributions of eddy kinetic energy throughout the water column. Comparison to theory and model output reveals a relationship between vertical structure and bathymetry. These results show that vertical structures vary significantly with bathymetry, density stratification, and latitude and contribute to model development efforts to reproduce the effects of eddy turbulence without explicit representation. These results also enhance interpretations of more numerous surface observations.

KEYWORDS: Mesoscale processes; Ocean dynamics; Turbulence; Energy transport; In situ oceanic observations; Climate models

1. Introduction

Since their first four-dimensional characterization in the Mid-ocean Dynamics Experiment (MODE-Group 1978), mesoscale eddies have been recognized as playing an important role in ocean mixing (Groeskamp et al. 2020), ocean heat content change (Kamenkovich et al. 2017; Jing et al. 2020; Siegelman et al. 2020), meridional heat transport (Zhao et al. 2018a), tracer advection [e.g., carbon transport/export (Harrison et al. 2018)], and the regulation of nutrient supply driving primary productivity (Mahadevan et al. 2012; Patel et al. 2020). This results in part because the mesoscale eddy field contains a majority of oceanic kinetic energy (Wunsch and Ferrari 2004), converted from available potential energy via baroclinic instability (Gill et al. 1974; Smith 2007). The mesoscale eddy field typically encompasses motions with horizontal length scales from tens to hundreds of kilometers evolving on time scales of days to months and includes time-dependent motions such as meanders and coherent vortices. Importantly, horizontal eddy length scales decrease with increasing latitude (Klocker et al. 2016), presenting a contemporary challenge in ocean modeling efforts to resolve and/or and parameterize key eddy processes (Hallberg 2013; Fox-Kemper et al. 2019).

Past observations and studies of mesoscale eddies have often focused on the surface or upper ocean (e.g., Chelton et al. 2011). Where subsurface measurements have been collected, they typically reflect short periods of intense vertical profiling or long-term monitoring at fixed locations with limited vertical resolution (Wunsch 1997; de La Lama et al. 2016). Historically, long-term in situ observations (i.e., moorings) have been instrumented with only a handful of sensors spanning the full water column (e.g., Rocha et al. 2014; Zhao et al. 2018b). This has limited our understanding of eddy vertical structure and the variations in mesoscale eddy kinetic energy with depth, as well as complicated efforts to determine geographic variability and the physical controls on vertical structure.

Denotes content that is immediately available upon publication as open access.

Corresponding author: Jacob Steinberg, jacob.steinberg@noaa.gov

DOI: 10.1175/JPO-D-25-0044.1

Understanding the factors that set and control the vertical structure of the mesoscale eddy field is, however, of significant importance from an ocean energetics perspective, as their turbulent interactions result in the transfer of kinetic energy out of the upper ocean and into the deep ocean. A central feature of mesoscale, or geostrophic, turbulence is the upscale transfer of energy to larger horizontal and vertical scales (Charney 1971). It is this transfer of energy to larger vertical scales that results in energy transfers from the surface to the deeper ocean, enabling mesoscale eddy influence on large-scale circulation and heat transport. Processes that either enhance or inhibit such transfers need to be better understood. The varied geography of eddy vertical structure has only recently been considered with increased detail (de La Lama et al. 2016; LaCasce 2017; Groeskamp et al. 2020) and continued investigation into the physical processes moderating vertical structure and its evolution is needed. One important application of such an analysis would be to infer vertical structure from remotely sensed sea surface height measurements.

Quasi-two-dimensional geostrophic turbulence theory offers an understanding of how mesoscale eddy kinetic energy (EKE), generated via baroclinic instability largely confined to the upper ocean (Smith 2007), is transferred across vertical scales (Charney 1971; Rhines 1979; Fu and Flierl 1980; Hua and Haidvogel 1986; Smith and Vallis 2001). These theories principally reveal vertical structure dependence on latitude and vertical density stratification, while assuming a flat ocean seafloor. At a high level, Klocker et al. (2016) describe this landscape of geographic turbulence as a transition from a zonostrophic turbulence regime at the equator to a vortex gas regime at the poles (Larichev and Held 1995; Held and Larichev 1996; Gallet and Ferrari 2021). The zonostrophic regime is characterized by zonal jets that form as a result of little horizontal-scale separation between the first baroclinic Rossby radius of deformation and the Rhines scale, scales at which instabilities adjust and feel changes in Earth's rotation, respectively. The vortex gas regime is characterized by relatively smaller coherent vortices that do not feel latitudinal changes in the Coriolis parameter.

The separate but compounding effects of sloping and/or rough bathymetry in moderating vertical structure have more recently been considered by de La Lama et al. (2016), LaCasce (2017), and LaCasce and Groeskamp (2020). Using a suite of observations, albeit with relatively coarse vertical resolution, these studies develop complementary theory and expectation that, in the presence of steeply sloping or rough bathymetry, eddy vertical structure should remain surface intensified rather than transfer to larger vertical scales or graver vertical modes (i.e., barotropize). In this work, the authors corroborate the theoretical results with the analysis of the observed eddy vertical structure and show that inferred "surface mode" or "rough-bottom mode" vertical structures both are realistic and can be used to improve eddy parameterizations in global ocean simulations [e.g., as in Groeskamp et al. (2020) and Yankovsky et al. (2024)]. de La Lama et al. (2016) and LaCasce (2017) specifically discuss the sensitivity of eddy vertical structure to slope magnitude and orientation relative to the eddy propagation direction and suggest the approximation of zero or near-zero horizontal velocity near the seafloor as often appropriate and expedient. They demonstrate how the traditional barotropic vertical structure, relating to nonzero near-bottom velocities, is modified to represent bottom-trapped topographically steered Rossby waves, a mechanistic pathway to bottom dissipation.

Similar eddy vertical structures have been derived from surface quasigeostrophic theory (Lapeyre and Klein 2006), emphasizing the nonlocal vertical influence of surface buoyancy anomalies and the general decay of horizontal velocity with increasing depth (e.g., Zhang et al. 2024) over the upper few hundred meters (LaCasce and Mahadevan 2006; LaCasce and Wang 2015). Eddy vertical structure is also influenced by mean flow vertical structure and velocity shear. Beckmann (1988) and Brink and Pedlosky (2020) derive vertical modes in the presence of mean flow, discuss stability criteria, and reveal how the vertical tilting of mode structures coincides with horizontal length scale changes. These efforts all modify traditional expectation that vertical structure can be universally characterized using flat-bottom dynamical modes and show that the vertical distribution of kinetic energy is geographically varied and influenced by surface conditions, background flow structure, and seafloor geometry.

As part of the Climate Process Team on Ocean Transport and Eddy Energy (Zanna et al. 2019), and with the goal of improving mesoscale eddy parameterizations in global climate models, this work leverages both observations and model output to further investigate the relationship between eddy vertical structure and varied ocean bathymetry, particularly without making a priori assumptions (e.g., assuming a decrease in horizontal velocity with increasing depth). We build on the recent results of Toole et al. (2023) that reveal no universal mesoscale vertical structure and undertake an expanded analysis of variability at four mooring sites that includes consideration of energy partitioning as a function of depth and time. Here, we further evaluate these high-resolution mooring observations alongside eddy vertical structure in a high-resolution climate model. Common methods used to characterize vertical structure are introduced and first applied to describe eddy vertical structure at four ocean mooring sites (section 3). With these methods of characterization, a high-resolution (0.1°) coupled atmosphere–ocean climate model [National Oceanic and Atmospheric Administration: Geophysical Fluid Dynamics Laboratory's Climate Model, version 2.6 (CM2.6)] is employed to investigate the geographic diversity in vertical structure and consider relationships to bathymetric slope and roughness (section 4). The results are discussed in the context of geostrophic turbulence expectations, and conclusions reflect on opportunity to implement new parameterizations in coarser resolution climate models and to infer vertical structure from surface observations (section 5). This analysis reveals an empirical dependence of vertical structure on bathymetric slope and roughness that only appears at high latitudes and where the seafloor is relatively flat and smooth. Continued evaluation of these relationships should inform ongoing model development and enable the assessment of geographically varying vertical structure.

TABLE 1. OOI mooring site name, latitude, longitude, seafloor depth, deployment duration, [1° × 1°] bathymetric slope magnitude, and [1° × 1°] bathymetric roughness.

Site	Latitude	Longitude	Seafloor depth (H) (m)	Duration	Slope	Roughness (m)
SO	54°28.1′S	89°22.1′W	4800	17 Dec 2015–11 Sep 2017	2.1×10^{-3}	253
ArgB	42°58.9′S	42°29.9′W	5200	17 Mar 2015–11 Mar 2016	3.9×10^{-5}	61
Irm	59°58.5′N	39°28.9′W	2800	12 Sep 2014–19 Sep 2016	5.8×10^{-3}	136
Papa	50°4.2′N	144°47.9′W	4700	5 Jun 2015–23 Mar 2016	1.9×10^{-3}	316

2. Observations and model output

a. *Ocean Observatories Initiative moorings*

Between 2014 and 2018, ocean moorings were deployed at four sites as part of the Ocean Observatories Initiative (OOI) (Cowles et al. 2010; Toole et al. 2023) (Table 1), observing near full-depth horizontal velocity and density evolution for multiyear periods. Measurements were made by either one or two autonomous McLane Moored Profilers, sampling on a daily basis from $\sim z = -250$ m to within 100 m of the seafloor. High vertical resolution $\mathcal{O}(1)$ m enabled the characterization of higher mode, or smaller vertical scale, eddy perturbations throughout the entire water column.

Measurements of zonal velocity u, meridional velocity v, temperature T, and salinity S were first processed to 1/2 dbar (~0.5 m) vertical resolution and daily temporal resolution as in Toole et al. (2023). Daily gridded sea surface velocities derived from satellite altimeter measurements from the Copernicus Marine Service (CMEMS 2024) were first linearly interpolated to each central mooring site location. Surface velocities were then linearly interpolated in depth from the surface down to the shallowest mooring velocity observation at ~250 m [a procedure slightly different from Toole et al. (2023), taken to avoid the complexity of processing upper-ocean current measurements from moorings tens of kilometers away]. These "complete" full-depth horizontal velocity profiles were then averaged over 5-day periods to remove superinertial motions and match the temporal resolution of CM2.6 (Fig. 1). While these preprocessing steps are slightly different than Toole et al. (2023), modes of eddy vertical structure variability, derived in the next section, are qualitatively no different than their results as less than 10% of each profile is interpolated. The same procedure was carried out to construct full-depth temperature and salinity profiles using up-to-date gridded fields derived from Argo profiling float measurements (Roemmich and Gilson 2009). Time-mean densities, averaged over full deployment periods, $\overline{\rho}(z)$ were calculated using the Gibbs Seawater Package.

b. *NOAA GFDL CM2.6*

To enable a more comprehensive investigation of the relationship between eddy vertical structure and bathymetry, we use the National Oceanic and Atmospheric Administration: Geophysical Fluid Dynamics Laboratory (NOAA GFDL) CM2.6 coupled ocean–atmosphere simulation (Delworth et al. 2006; Gnanadesikan et al. 2006; Delworth et al. 2012; Zhang and Delworth 2015; Griffies et al. 2015). This simulation was selected as it is one of a few global atmosphere–ocean coupled eddy-resolving simulations run for hundreds of years. This simulation was run using the Modular Ocean Model, version 5 (MOM5), with 0.1° horizontal ocean resolution and 50 vertical levels (Griffies 2012). No mesoscale eddy parameterization was used in this configuration, and the Hallberg (2013) criteria of two model grid points per deformation scale are met equatorward of ~65°N/S and at depths greater than ~1500 m (Hallberg 2013). The results like those from Chelton et al. (2011) show dominant eddy scales to be larger than deformation radii, suggesting this may be a conservative estimate of the extent over which mesoscale features are resolved. In the subsequent analysis, we extract and use 5-day-mean full-depth horizontal velocities spanning the last 2 years of the 200-yr-long preindustrial control run. This run was selected to withhold consideration of changing eddy structure and activity in the presence of current and future ocean warming, a topic to be considered in future work. This choice has some implications for subsequent comparison to observations, as the real ocean stratification over the upper few hundred meters has changed with increased ocean heat uptake (Li et al. 2020), but these comparisons are made primarily to gauge model fidelity rather than closely assess model-observation differences.

3. Analysis framework: Characterization of bathymetry and vertical structure

a. *Stratification, bathymetric slope, and bathymetric roughness*

We first define stratification and seafloor characteristic metrics to be used in the subsequent evaluation of eddy vertical structure (Fig. 2). With CM2.6 output, we calculate the time-mean depth-averaged Brunt–Väisälä frequency N divided by the local Coriolis frequency f at every fifth horizontal grid index. This decimation procedure is subsequently adopted in the evaluation of model output to decrease calculation run times. When multiplied by a scale height, this ratio is the first baroclinic Rossby radius of deformation, a horizontal length scale associated with baroclinic instability. On its own, it is a unitless characterization of the rate of decay of density with increasing depth that takes into account the influence of Earth's rotation on eddy dynamics. Values generally decrease with increasing latitude, a result of weaker stratification at high latitudes and larger values of the Coriolis frequency. Some zonal variations in this ratio appear at higher latitudes, with the Labrador Sea (≈55°N, 50°W), Amundsen Sea (≈65°S, 120°W), and Enderby Plain (≈65°S, 40°E) all noticeable.

At model grid points and mooring locations, zonal and meridional bathymetric slopes are calculated from a [1° × 1°]

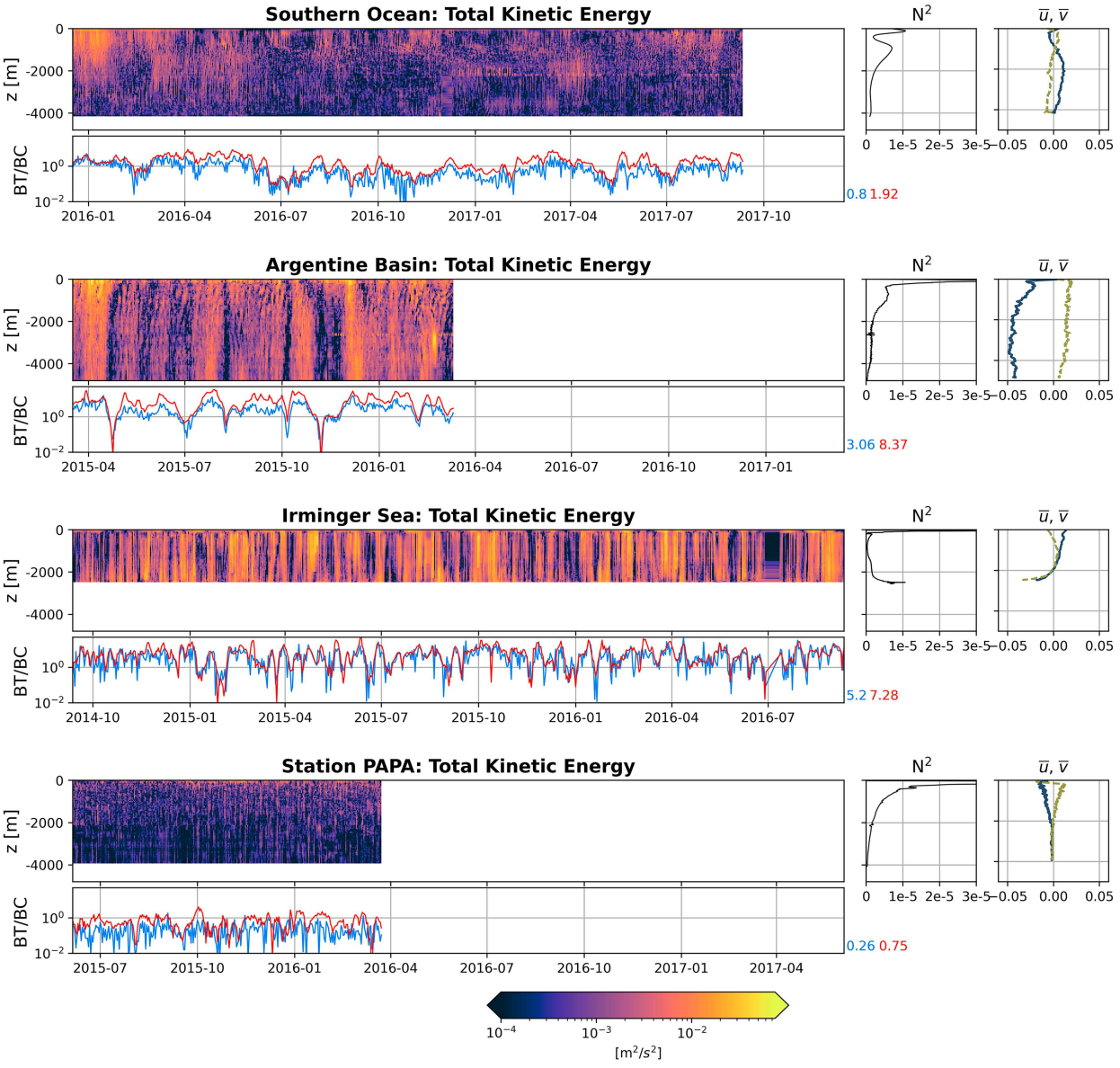

FIG. 1. TKE [KE = (1/2)(u^2 + v^2)] as a function of depth and time at each OOI mooring site. For each site, the right columns are the annual mean stratification [$N^2 = -(g/\rho_0)(\partial\overline{\rho}/\partial z)$ (g = 9.8 m s^{-2}, ρ_0 = 1035 kg m^3) (s^{-2})] and total time-mean zonal $\overline{u}$ (blue) and meridional $\overline{v}$ (yellow) velocity (m s^{-1}). Secondary rows are BT-to-BC TKE ratios at mooring vertical–temporal resolution (blue) and model vertical–temporal resolution (red). Red and blue text are the time-mean of each ratio.

planar fit, centered at the relevant grid point or mooring location. The slope magnitude is defined as $\sqrt{(\partial H/\partial x)^2 + (\partial H/\partial y)^2}$, where H is the seafloor depth. Bathymetric roughness is defined as the root-mean-square difference between bathymetry over this 1° × 1° region and the planar fit. Slope and roughness are calculated from model partial step bathymetry at 0.1° resolution, generated from multiple datasets (Griffies et al. 2005), with 100 points used in each planar fit. At each of the four mooring sites, a 1-min resolution global seafloor topography dataset was used (Smith and Sandwell 1997). The 1° scale is chosen to evaluate bathymetry as it falls within the range of horizontal length scales associated with the mesoscale features of interest in this study (equivalent calculations were carried out across 50- and 150-km-wide boxes with no significant difference in results). Roughness can then be thought of as a metric of bathymetric variability across an eddy length scale that may influence eddy structure and behavior.

Midocean ridges and continental slopes stand out as steeply sloped, and while the spatial patterns of roughness appear similar to that of slope, a secondary peak in the roughness distribution reveals distinct low roughness areas (Figs. 2d,f). In a handful of regions, including seas surrounding Antarctica (south of ≈50°S), the Argentine Basin (≈45°S, 45°W), the western

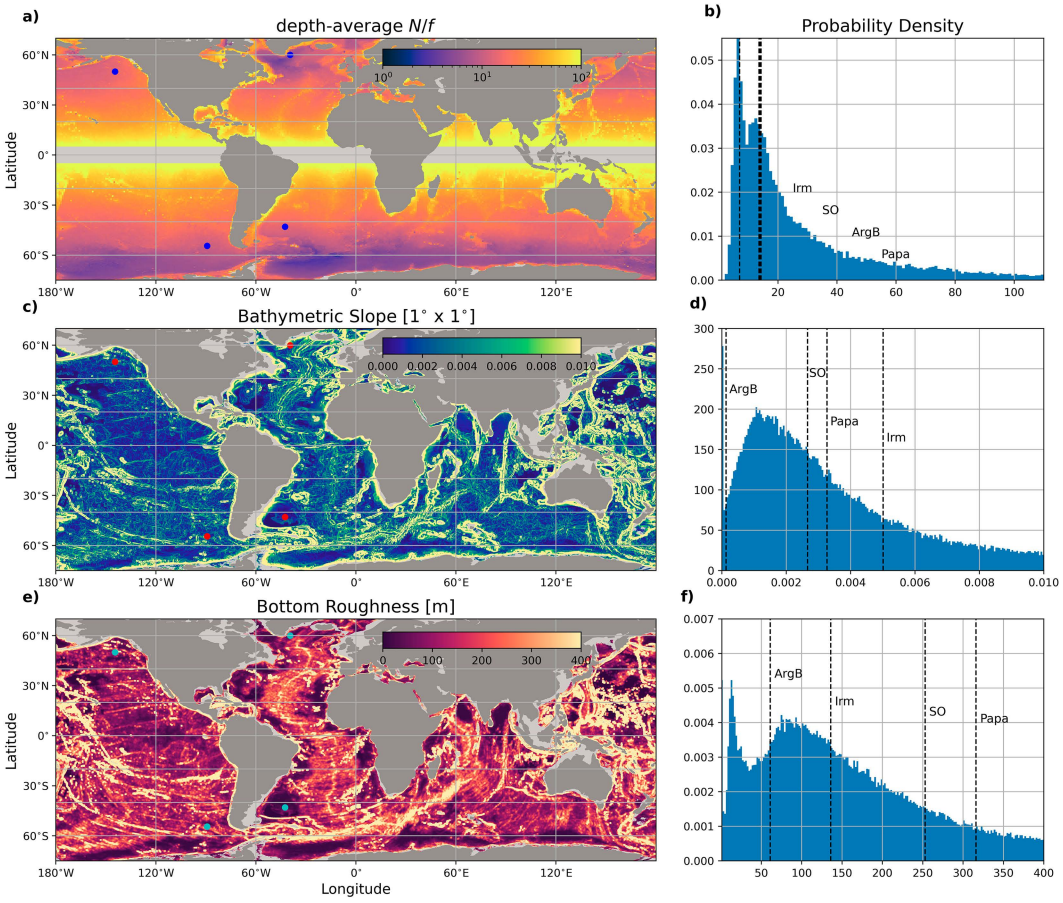

FIG. 2. NOAA GFDL's CM2.6: (a) Depth-averaged Brunt–Väisälä frequency N divided by the local Coriolis frequency f (values are omitted within 5° of the equator). (b) Probability density function of N/f with vertical dashed lines identifying the mooring site values. Where dashed lines overlap, sites are listed in increasing order. (c),(d) As in (a) and (b), but for [1° × 1°] bathymetric slope magnitude. (e),(f) As in (a) and (b), but for [1° × 1°] bottom roughness, defined as the root-mean-square of the difference between a [1° × 1°] planar fit and 1/10° resolution bathymetry. In (a), (c), and (e), the scattered points identify the locations of the four OOI mooring sites.

North Atlantic abyssal plain (≈30°N, 70°W), and Labrador Sea (≈55°N, 50°W), the seafloor is over an order of magnitude less steeply sloped and smoother than the global median of 3×10^{-3} and 143 m.

b. *Metrics of vertical structure*

Of the many methods that can be used to characterize the vertical structure of total kinetic energy (KE) and EKE, we calculate the barotropic to baroclinic KE and EKE ratios, the first two vertical empirical orthogonal functions (EOFs), and flat-/sloping-bottom dynamical vertical modes, as these collectively allow for eddy vertical structures to be considered from energetics and theory-based perspectives. Quasigeostrophic dynamical modes have typically been used to assess or prescribe the vertical partition of kinetic energy, to compare observations to theoretical expectations (e.g., Wunsch 1997; Steinberg and Eriksen 2022; Toole et al. 2023), or to infer vertical structure from upper-ocean or surface observations (e.g., McCoy et al. 2020). The fraction of barotropic EKE is a simple and commonly used metric that can also be used to infer the existence or extent of the inverse cascade in ocean simulations (Yankovsky et al. 2022). This metric cannot, however, reveal information about surface mode-like structures that project onto barotropic and first baroclinic flat-bottom modes in the presence of rough bathymetry. Nondynamically constrained EOFs add to these interpretations by revealing if and where vertical structures agree with theoretical expectation. They also provide a natural basis upon which to impose a vertical structure classification scheme and reveal the role bathymetry plays in moderating the vertical distribution of EKE. The remainder of this section describes these three methods of characterization.

1) BAROTROPIC TO BAROCLINIC KINETIC AND EDDY KINETIC ENERGY RATIOS

The total KE (TKE) and EKE vertical structure can first be partitioned into and characterized using depth-independent (barotropic) and depth-varying (baroclinic) components. For EKE, we take a traditional approach and explicitly define

zonal and meridional eddy velocities as anomalies with respect to a local time mean over the 2 years of model output or length of the observational record ($u' = u - \overline{u}$, $v' = v - \overline{v}$, where the overbar denotes the time mean). Using perturbation velocities facilitates the comparison to horizontal velocity EOFs. The respective barotropic (BT) and baroclinic (BC) EKE terms are written as

$$\mathrm{EKE_{BT}} = \frac{1}{2H}\left(\int_{z=-H}^{z=0} u'\,dz\right)^2 + \frac{1}{2H}\left(\int_{z=-H}^{z=0} v'\,dz\right)^2, \tag{1}$$

$$\mathrm{EKE_{BC}} = \frac{1}{2H}\left[\int_{z=-H}^{z=0}\left(u' - \frac{1}{H}\int_{z=-H}^{z=0} u'\,dz\right)^2 dz + \int_{z=-H}^{z=0}\left(v' - \int_{z=-H}^{z=0} v'\,dz\right)^2 dz\right]. \tag{2}$$

In this formulation, integrals of the cross terms between $\overline{u}$ and u' and $\overline{v}$ and v' are not considered but average to zero if uncorrelated. The same expressions were used to calculate the time-varying ratio of TKE using full velocity fields (Fig. 1).

2) EOFs

EOFs were calculated at each mooring site and every fifth model grid point and represent the dominant vertical modes of inherent horizontal velocity variability. Typically, the first few EOFs can explain a significant fraction of horizontal velocity variability. EOFs are determined by solving the general eigenvalue problem

$$\mathbf{A}\phi = \Lambda\phi, \tag{3}$$

where the covariance matrix $\mathbf{A} = (\mathbf{U}')(\mathbf{U}')^{\mathrm{T}}$ is constructed of horizontal velocity anomalies $\mathbf{U}'$ (a function of depth and time), ϕ are the eigenfunctions referred to as EOFs, and Λ are the eigenvalues describing the fraction of variance explained by each ith eigenfunction ($\Lambda_i^2/\sum_{i=1}^{N}\Lambda_i^2$).

3) Quasigeostrophic dynamical modes

Finally, both flat-bottom and sloping-bottom quasigeostrophic dynamical modes Φ are calculated as a qualitative reference in the interpretation of EOF vertical structure and to highlight the sensitivity of sloping-bottom modal structure to bathymetric slope and eddy propagation direction (Fig. 3). These modes describe the vertical structure of the geostrophic streamfunction $\Psi = a(t)\Phi(z)e^{i(kx+ly-\omega t)}$, where $a(t)$ are the mode amplitudes, k and l are the zonal and meridional horizontal wavenumbers, and ω is the frequency (Wunsch and Stammer 1997). Vertical mode solutions are obtained for m modes solving the Sturm–Liouville second-order ordinary differential equation,

$$\frac{d}{dz}\left(\frac{N^2}{f_0^2}\frac{d\Phi}{dz}\right) + \lambda^2\Phi = 0, \tag{4}$$

where N^2 is the site-specific time-mean vertical profile of stratification, f_0 is the local Coriolis parameter, and λ is the eigenvalues (Wunsch 1997). In the flat-bottom case, these vertical modes are a function of depth alone, but like EOFs, their expression can vary in time when scaled by amplitude $a(t)$. At any time, horizontal velocity can be reconstructed as the sum of each mth mode multiplied by its time-varying amplitude. Mode solutions are obtained assuming a rigid-lid $[(d\Phi/dz)|_{z=0} = 0]$ surface boundary condition and both flat- and sloping-bottom boundary conditions. The flat-bottom boundary condition assumes no vertical velocity at the sea floor,

$$\left.\frac{d\Phi}{dz}\right|_{z=-H} = 0, \tag{5}$$

while horizontal velocities can be nonzero. Sloping-bottom modes, derived by Toole et al. (2023) expanding on LaCasce (2017), alter this bottom boundary condition as

$$\left.\frac{d\Phi}{dz}\right|_{z=-H} = \Phi\frac{N^2}{\beta f_0}\left(\gamma\frac{l}{k} - \alpha\right)(k^2 + l^2 + \lambda^2), \tag{6}$$

requiring no flow normal to a sloping seafloor. Here, α and γ are the linear meridional and zonal slopes [$H = H_0 - h(x, y)$, $h = \gamma x + \alpha y$], $\beta = df/dy$, and k and l are the zonal and meridional wavenumbers, respectively. These solutions reveal modal structure to depend on bathymetric slope, horizontal wavenumber, and azimuth of propagation relative to bathymetric slope. As slopes steepen to absolute values greater than $\sim 10^{-4}$, these modal structures become less dependent on horizontal wavenumber and decay with increasing depth to near-zero amplitude at the seafloor. This structure is evident at the Southern Ocean site where bathymetry is both moderately sloped and rough (Figs. 3a–c). In the limit of a flattening bathymetric slope, sloping-bottom mode solutions collapse onto the flat-bottom mode solutions and become independent of the horizontal wavenumber. At the Argentine Basin site, where the seafloor slope is over an order of magnitude less than at the Southern Ocean site, both sloping and flat-bottom modes appear similar to little wavenumber dependence (Figs. 3d–f). Consideration of a transition from sloping to flat-bottom modes with decreasing bathymetric slope suggests the strongest horizontal wavenumber dependence for moderate slopes or values roughly coinciding with the peak in the slope distribution (Fig. 2d). It should also be noted that these solutions assume a constant slope and in the presence of roughness, and vertical structures should become more surface trapped (LaCasce and Groeskamp 2020).

While dynamical modes can be difficult to calculate and may be dependent on bathymetry and/or eddy characteristics, they can be useful in prescribing dynamically relevant vertical structure of eddy diffusivity or kinetic energy backscatter in ocean model parameterizations. This is especially the case in regions of either very flat or steeply sloped bathymetry. Projection of velocity profiles onto these modes also affords opportunity to compare the vertical wavenumber spectrum to that predicted by quasigeostrophic turbulence theory (e.g., Charney 1971). In energetic regions of the ocean, the prediction of a -3 dependence of the kinetic energy spectrum on the vertical wavenumber could be expected (Wang et al. 2010; Xu and Fu 2011)

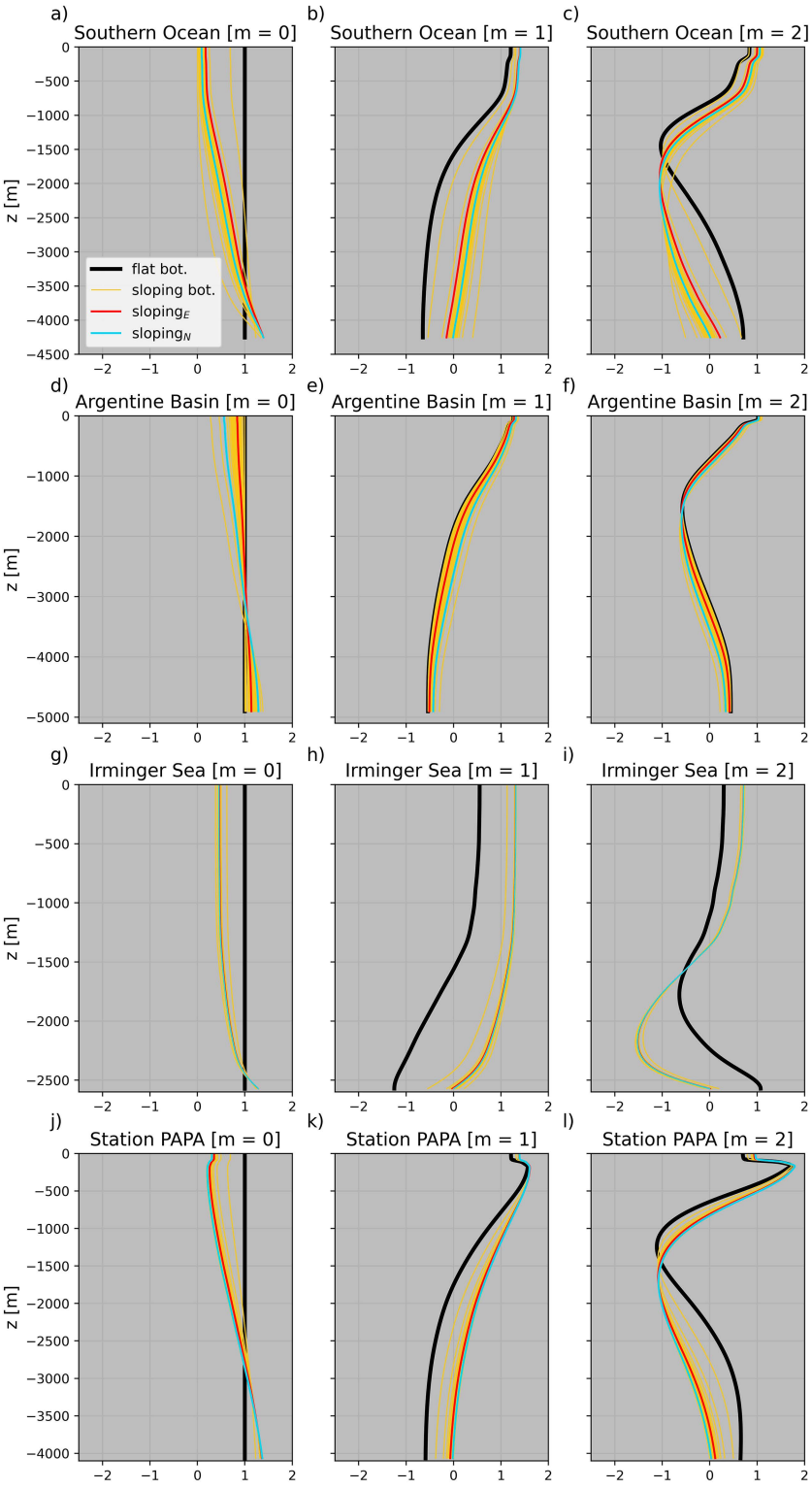

FIG. 3. (a)–(c) First three flat (black) and sloping (yellow) bottom modes Φ at SO. Mode amplitudes are scaled to physical units based on the derived variance. Sloping-bottom mode solutions are shown for a 100-km horizontal wavelength and across 70 azimuths evenly spaced between 0° and 360°. Profiles in red and blue identify the mode solutions corresponding to east and north azimuths. First three flat- and sloping-bottom modes at (d)–(f) ArgB, (g)–(i) Irm, and (j)–(l) Papa.

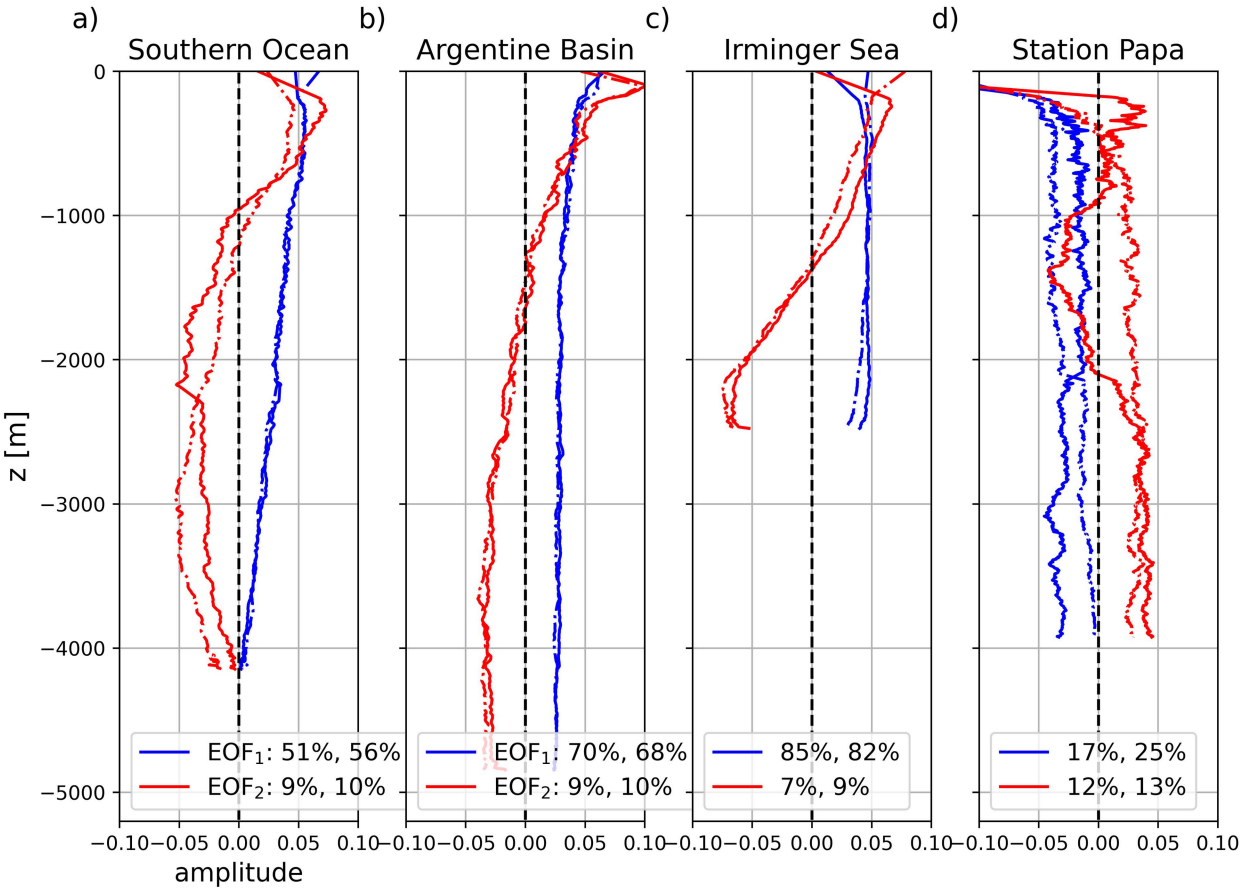

FIG. 4. First (blue) and second (red) horizontal velocity EOFs at each OOI mooring site for zonal (solid) and meridional (dashed) velocity. EOFs are calculated from daily velocity time series. The legend includes the percent variance explained by each (zonal and meridional) EOF.

where turbulence theory-based assumptions are met (Steinberg and Eriksen 2022) and the seafloor is flat.

4. Results

a. Observations

Time-mean $(\overline{u}, \overline{v})$ and time-varying (u', v') horizontal velocity structures at each of the four sites are all distinct (Fig. 1). At the Southern Ocean (SO) site, total kinetic energy is largely surface intensified; mean stratification is nonmonotonic with depth, highlighting a subthermocline secondary maximum; and mean flows are relatively weak. In contrast, vertical structures at the Argentine Basin (ArgB) site are largely uniform in depth with relatively strong, weakly sheared westward/north-westward mean flows. The Irminger Sea (Irm) site, along the Greenland continental slope, is relatively shallow with barotropic-like structures and near-bottom intensified flow and stratification. Finally, Station Papa (Papa) is relatively quiet with weak mean flows at all depths. These unique density and flow features are paired with site unique bathymetry. Both SO and Papa are relatively average in slope with higher roughness, while ArgB is notably flat and smooth and Irm is steeply sloped and moderately smooth [Fig. 2; see also Toole et al. (2023), appendixes a–d].

With the exception of Papa, the first two zonal and meridional velocity EOFs at each site together explain a majority of horizontal velocity variance (greater than 60%, Fig. 4). These EOFs highlight the extent to which mesoscale eddy vertical structures depend on depth. At SO, these EOFs bear marked resemblance to the first and second sloping-bottom baroclinic modes (e.g., LaCasce 2017, Figs. 3b,c), while at ArgB, these EOFs appear similar to the zeroth and first flat-bottom modes (Figs. 3d,e). Upper-ocean stratification is greater at ArgB, which could lead to the expectation that eddy vertical structure is more baroclinic, but site bathymetry is markedly flatter and smoother and thus apparently permits more barotropic motions (Fig. 2). For the mild slopes at Argb, sloping-bottom mode solutions are nearly the same as flat-bottom mode solutions, highlighting this site's decreased dependence of vertical structure on bathymetry and the wavenumber. We acknowledge the resemblance to the first surface mode with weakly sheared bottom flow but leave the influence of sheared flows for future work. These contrasting structures at SO and ArgB, and apparent agreement with different theoretical constructs, suggest that bottom slope and roughness are influencing factors that moderate local vertical

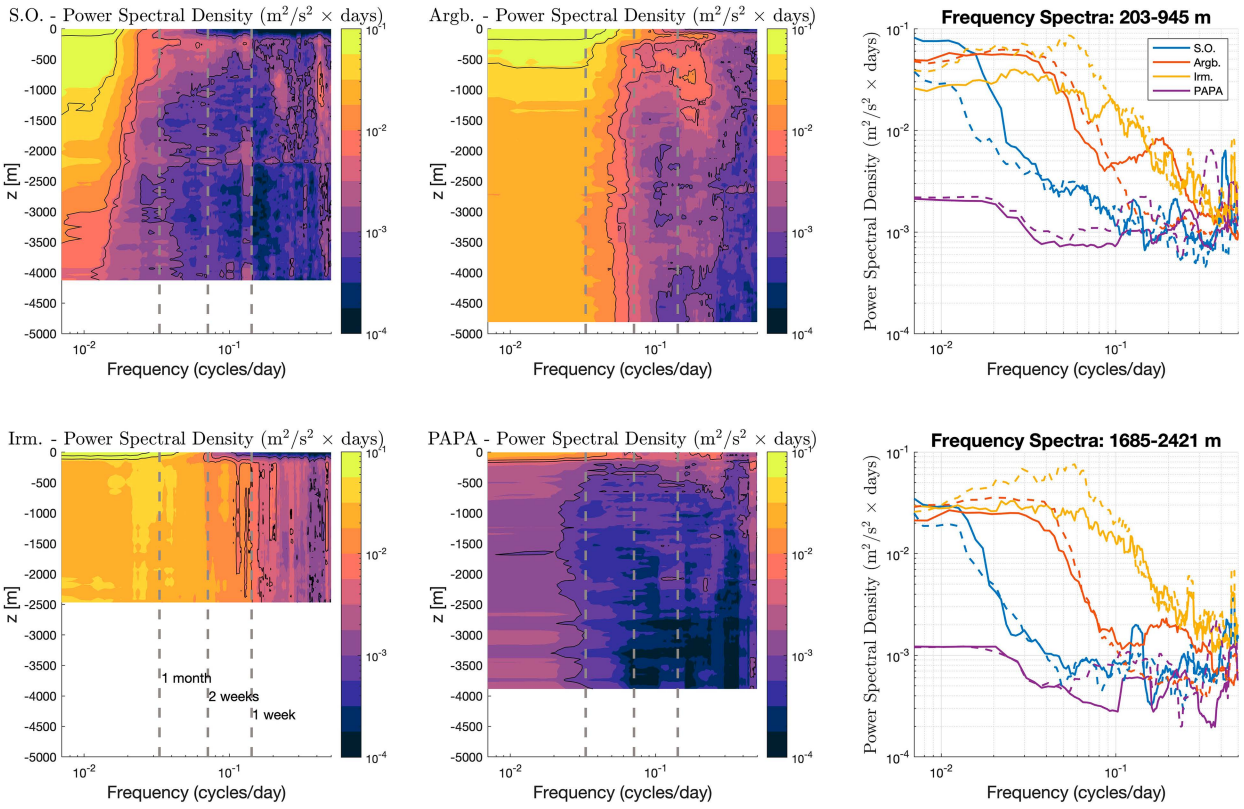

FIG. 5. Negative rotary frequency spectra at each OOI mooring site calculated from daily velocity profiles. Vertical dashed lines are 1-month, 2-week, and 1-week frequencies. (right) Frequency spectra averaged over shallow (~200–1000 m) and deep (~1700–2500 m) depth bands. The dashed lines are positive rotary spectra. Negative and positive spectra, respectively, represent the motions with clockwise and counterclockwise rotation.

structure throughout the water column, not just near the seafloor.

Vertical structures at Irm, along the continental slope of Greenland and within a boundary current, appear more similar to flat-bottom modes (Figs. 3g–i). While this may at first seem unexpected for its location on a slope, flat-bottom mode-like structures may be expected where eddy propagation follows isobaths (Toole et al. 2023), as is observed here (Zou et al. 2021), and horizontal wavelengths are sufficiently large. This expectation derives from acknowledgment that wave propagation and currents parallel the bathymetric gradient and $l/k = \alpha/\gamma$ [see Eq. (6)]. We again acknowledge that mean flows may alter and/or couple mode structures (Killworth et al. 1997) but reserve this consideration for future work. Papa is unique among the four sites as the first two EOFs explain less than 50% of velocity variance. Here, mesoscale eddy activity is weak and flows are likely impacted by nearby seamounts that extend to within ~1000 m of the surface (Pelland et al. 2016).

The diversity of mesoscale eddy structures among these four sites is likewise seen in considering frequency content as a function of depth (Fig. 5). At all sites and all depths, rotary frequency spectra are red, with greater energy observed at lower frequencies. At SO, between 1-week and ~2-month time scales, energy decreases with increasing depth by over one order of magnitude. In contrast, across these same frequencies, little decay with depth is observed at ArgB. Here, where eddy activity is over an order of magnitude more energetic, vertical structures transition from baroclinic at the lowest frequencies to barotropic across the 2-week to 1-month frequencies, those associated with mesoscale eddy variability. This comparison reveals eddy activity at ArgB to be more barotropic across mesoscale frequencies, while at SO, eddy energy across all time scales is surface intensified. Irm exhibits variability that is largely independent of depth across all frequencies while Papa is the least energetic at all frequencies and all depths. The vertical structure at SO and ArgB sites stands in marked contrast despite their similar latitude and proximity to energetic currents. The vertical structures, which, respectively, resemble sloping and flat-bottom modes, motivate a subsequent investigation of the potentially dominant influence of bathymetry.

b. *CM2.6–mooring locations*

To assess this simulation's ability to represent eddy vertical structure, 2-yr time series were first extracted at each of the four OOI mooring site locations. Mean and perturbation kinetic energy metrics (Fig. 6) are markedly similar to observations (Fig. 1), after interpolating and smoothing observations to match the 5-day and 50 vertical level model resolution. Overall, the model is more energetic at locations of elevated observed EKE (e.g., ArgB and SO upper ocean) and less energetic in

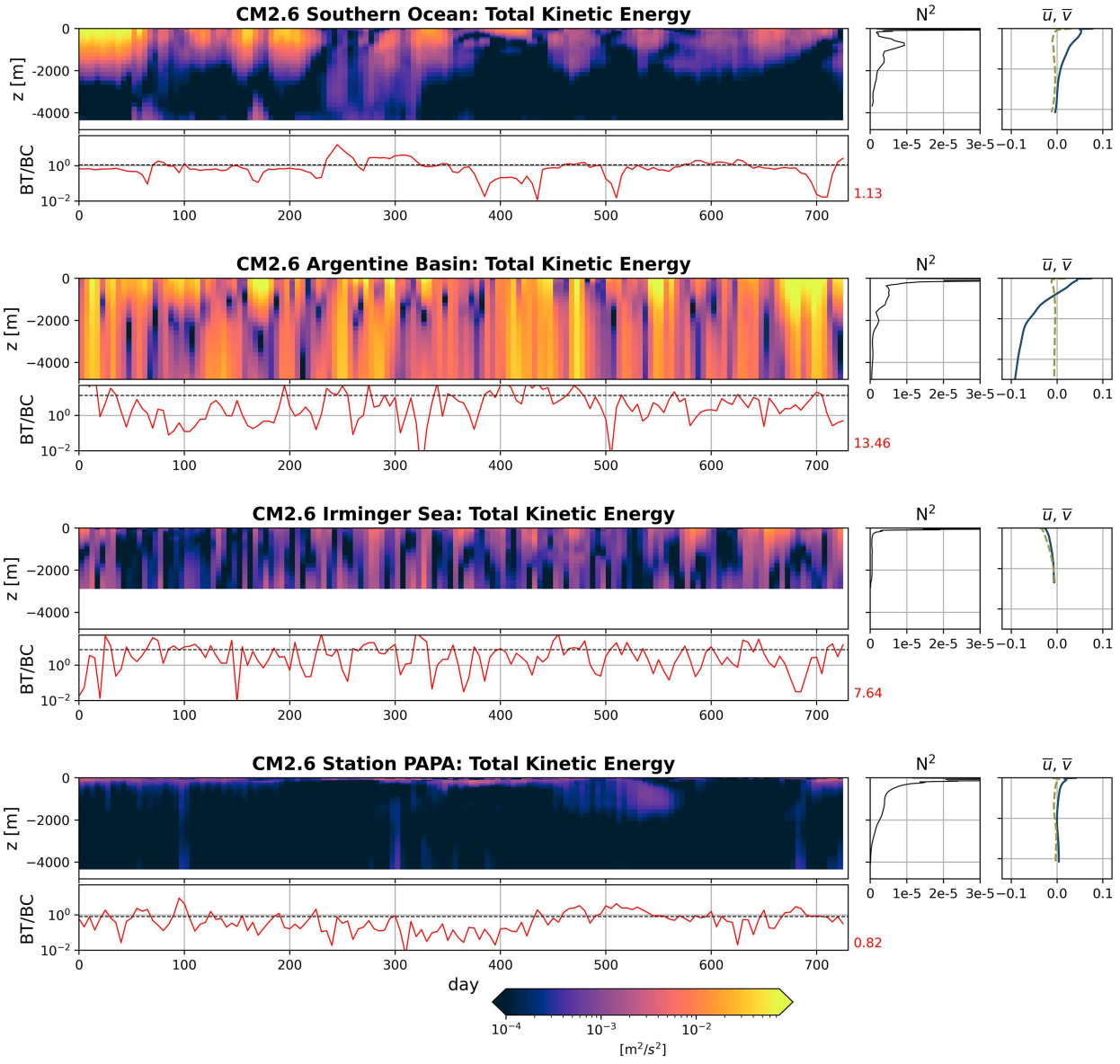

FIG. 6. TKE in depth and time at each OOI mooring site in CM2.6. As in Fig. 1, (right) and the secondary row for each site are mean stratification, zonal and meridional velocity, and the BT-to-BC KE ratio. The time-mean ratio is in dashed black. Note the different $\overline{u}$ and $\overline{v}$ profile horizontal axis limits as compared to Fig. 1.

quiet regions (e.g., Papa and SO deep ocean). Despite these differences, model vertical structures are dominantly barotropic at ArgB and Irm sites and dominantly baroclinic at the SO and Papa sites. This characterization is generally consistent with observations, but elevated mean flow shear in CM2.6 suggests model EKE to be overly baroclinic. Observed and modeled mean barotropic to baroclinic EKE ratios are (observed versus modeled) 1.9 versus 1.1, 8.4 versus 13.5, 7.3 versus 7.6, and 0.8 versus 0.8 at SO, ArgB, Irm, and Papa sites, respectively. Overall, these similarities suggest the model to well resolve the vertical structure of kinetic energy.

EOFs also compare favorably with observations (Fig. 7). At all sites, the first zonal and meridional velocity EOFs explain a majority of the velocity variance, with the observed EOF_1 percent variance explained increasing after interpolating in depth and averaging time to 5 days and 50 vertical levels (especially at Papa, see Figs. 4 and 7). With the exception of Papa, however, EOF_1 at CM2.6 mooring sites explains an even greater fraction of velocity variance, revealing that higher mode variability in the model is generally less well resolved. Importantly, model EOF_1 structures match observed EOF_1 structures in their rate of decay with increasing depth. As with the barotropic to baroclinic ratio characterization, this EOF approach reveals eddy velocities to decay with increasing depth at the SO site linearly to zero (largely baroclinic) and at the ArgB site to a near constant nonzero value (largely barotropic).

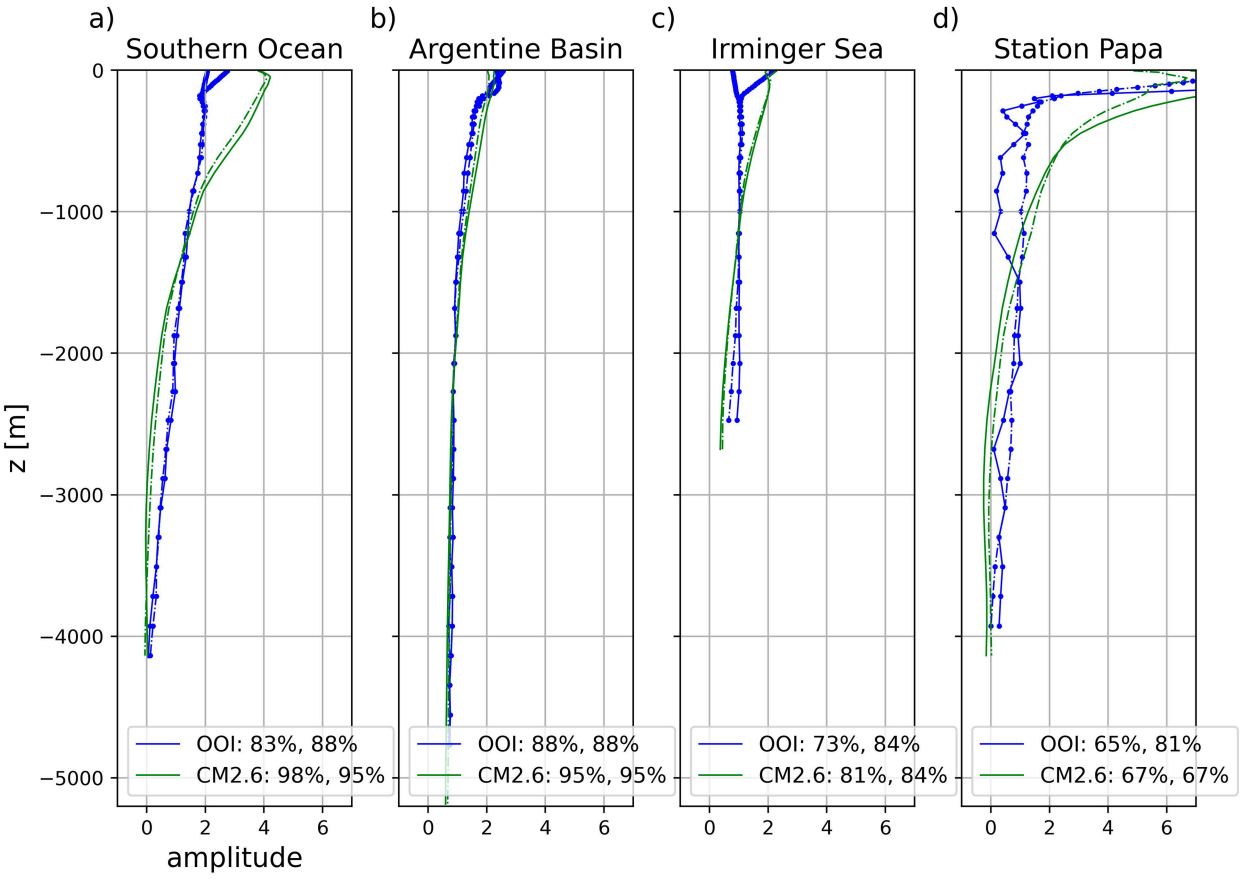

FIG. 7. Comparison of the first observed (blue) and modeled (green) horizontal velocity EOFs at each mooring site. Observed velocity profiles are averaged in depth and time to match the vertical–temporal resolution of CM2.6. Blue points along profiles denote the midpoint depth of each model layer. As in Fig. 4, the percent variance explained by each (zonal and meridional) EOF is added in the legend. The lines represent the zonal (solid) and meridional (dashed) EOFs.

These two sites are at a similar latitude and exhibit similar eddy activity but have a very different eddy vertical structure. To explore the role played by bathymetry in shaping these differences, we next evaluate the principal EOF structure globally.

c. *CM2.6–global*

While comparison between the observed and modeled vertical structure centered on total and eddy kinetic energy, we focus our global model vertical structure characterization on eddy kinetic energy. Barotropic to baroclinic EKE ratios, averaged in time [Eqs. (1) and (2) and Fig. 8], reveal a landscape in which eddy vertical structure becomes increasingly barotropic with increasing latitude. Zonal variability also increases with increasing latitude and reveals distinct regions where the barotropic EKE fraction is much greater than the baroclinic fraction (in contrast to low-latitude regions where this fraction is small and nearly constant across longitudes). Interestingly, these mid- and high-latitude regions of elevated barotropic EKE align with regions of flat bathymetry and low bathymetric roughness (Fig. 8). These regions include the Labrador Sea, Argentine Basin, and Antarctic adjacent abyssal plains (e.g., Weddell, Enderby, South Indian, Amundsen, and Bellingshausen). While an increase in the barotropic EKE fraction is to be expected in shallower regions, like the Arctic, many higher-latitude regions with elevated barotropic EKE are deeper than 4000 m (e.g., Argentine Basin and Enerby Plain). Excluding regions shallower than 1000 m, where continental shelf dynamics are distinct from mesoscale turbulence, the smoothest ~ 35% of ocean area is coincident with the ~75th percentile of BT/BC EKE. Restated, the smoothest 35% of the ocean aligns with the 25th percentile of the highest BT/BC EKE values.

These regions where the barotropic EKE fraction exceeds the baroclinic are also identifiable considering EOF_1 vertical structure. We calculate EOF_1 at every fifth model horizontal grid location and define a decay metric as the near-bottom (average magnitude over the deepest two model layers) to near-surface (average magnitude over the shallowest five model layers) ratio (Fig. 9a). While the depth range spanned by the deepest two model layers is a function of ocean depth, this range typically spans approximately 400 m. The surface five layers span approximately 50 m. If, at a single location, EOF_1 magnitude were constant with depth, like the zeroth flat-bottom dynamical mode, this ratio would equal one. Alternatively, if EOF_1 monotonically decays to zero with increasing depth,

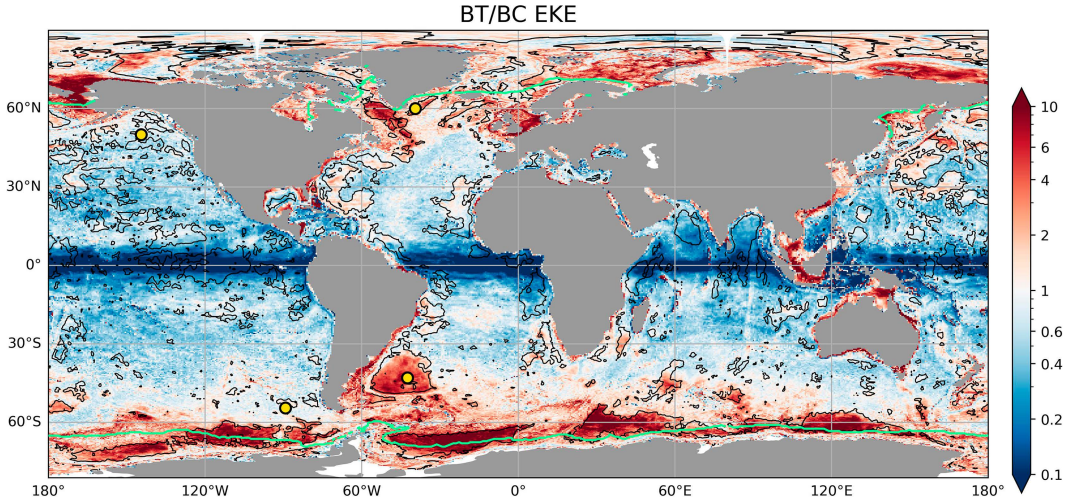

FIG. 8. Time-mean BT/BC EKE ratio plotted on a log color scale with a diverging colormap centered at a ratio of 1. Mooring sites are in yellow. A low bathymetric roughness value of 70 m is contoured in black (see Fig. 2 for distribution reference). The green contour identifies the equator-most extent of ocean area where sea ice is present for 50% or more of the year. In this figure alone, regions shallower than 1000 m are not excluded to highlight the dependence of this ratio on ocean depth.

this ratio would be near zero. Negative values correspond to the regions where EOF_1 changes the sign and vertical structure might be similar to the first baroclinic flat-bottom dynamic mode. This global characterization of the first EOF not only reveals eddy vertical structure to be dependent on latitude but also draws focus to the same distinct regions where the barotropic EKE fraction is elevated, as identified in Fig. 8.

Excluding locations near the equator where this first EOF explains less than 75% of meridional velocity variance (Fig. 9b), this EOF_1 decay metric is subsequently used to partition the ocean into four categories or regions of distinct vertical structure (Figs. 9c,d). The first is termed "baroclinic" and identifies equatorial and low-latitude regions where, like the first baroclinic flat-bottom mode, EOF_1 changes sign with increasing depth. Within this region, vertical structure assessment ensured

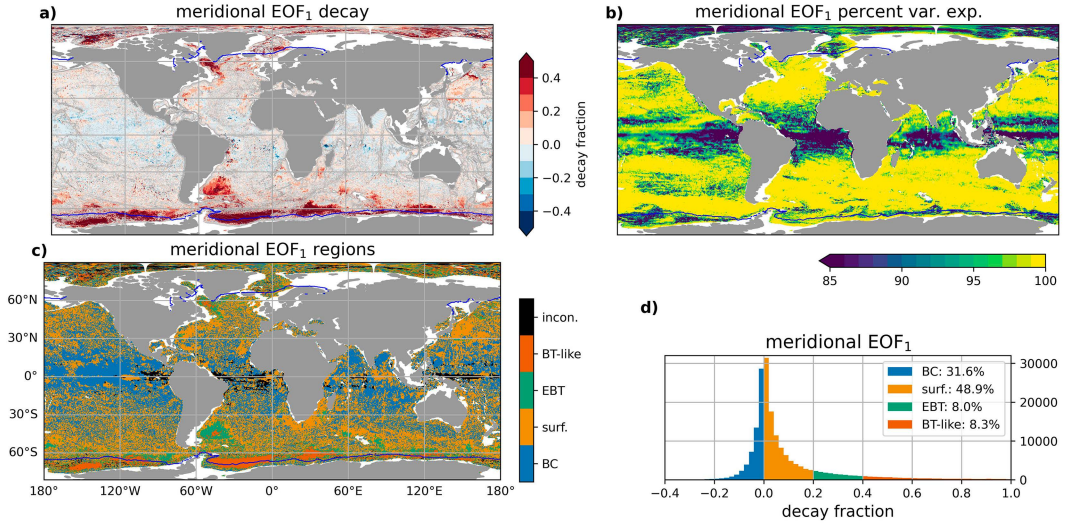

FIG. 9. (a) Vertical structure of meridional velocity EOF_1, termed EOF_1 decay and defined as the near-bottom to near-surface ratio. (b) Percent meridional velocity variance explained by EOF_1. (c) Five regions of the EOF_1 structure defined in section 4c: inconclusive (where EOF_1 explains less than 75% of velocity variance) (black), BT-like (orange), EBT (green), surface mode (yellow), and BC (blue). As in Fig. 8, the blue contour identifies the equator-most extent of ocean area where sea ice is present for 50% or more of the year. (d) Distribution of meridional EOF_1 decay fraction with category breakdown (plotted as gridcell count). Regions where the seafloor depth is less than 1000 m and where EOF_1 explains less than 75% of velocity variance are excluded.

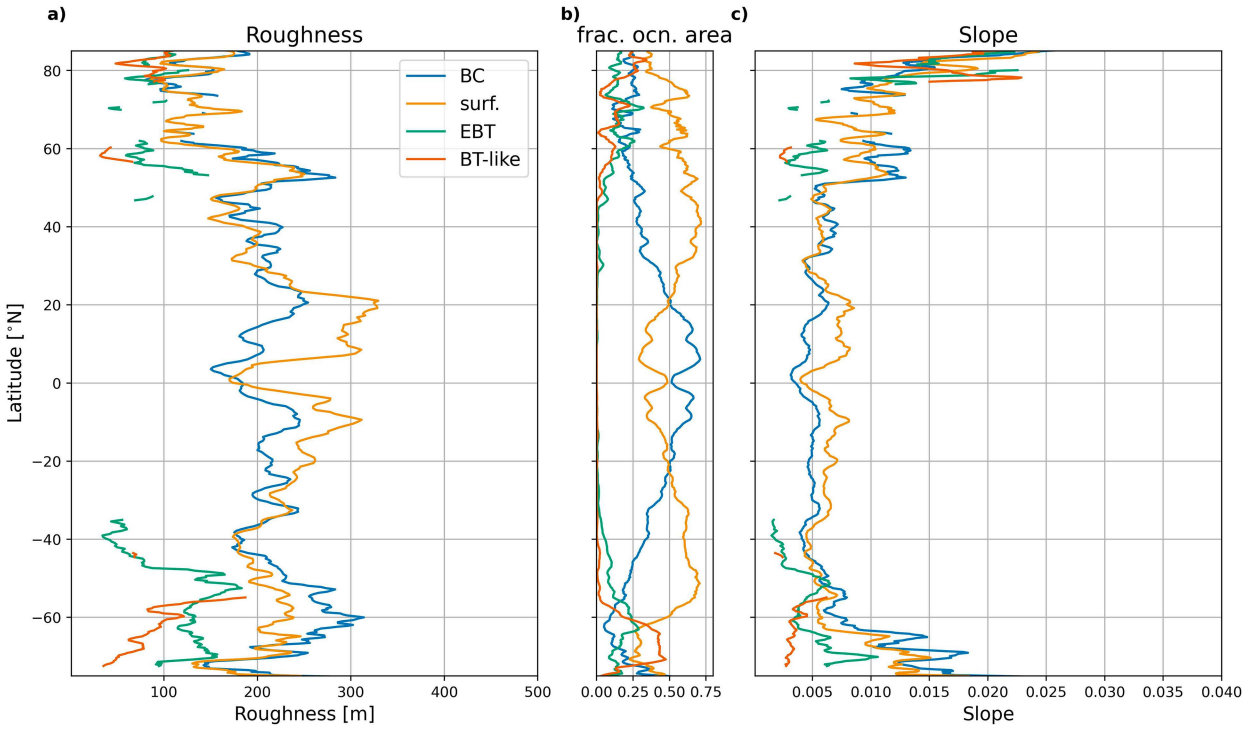

FIG. 10. (a) Zonal-mean roughness as a function of latitude and for each vertical structure category. (b) Fraction of ocean area at each latitude comprised by each category. (c) As in (a), but for bathymetric slope.

only one sign change in the vertical with the result that here, EOF_1 decay ratios are all negative. The second category defines eddy vertical structures as surface mode like, following the derivation and characterization of LaCasce (2017) and Toole et al. (2023). Here, the near-bottom EOF_1 magnitudes are no more than 20% of near-surface values. The third category is termed "equivalent barotropic" (EBT). Within these regions, eddy vertical structures decay with increasing depth to values between 20% and 40% of near-surface values. While these regions could be characterized as surface mode-like, near-bottom velocities are nonzero and poorly described by surface mode structure. The fourth category identifies regions where EOF_1 decay is weakest and vertical structures are most barotropic (i.e., EOF_1 decay ratios are greater than 0.4 and termed "barotropic-like"). These regions are largely found at higher latitudes and include the Labrador Sea and Argentine Basin. Together, EBT and barotropic-like regions comprise nearly 20% of total ocean area (Fig. 9d). Bathymetric slope and roughness values in these regions span the full range of model-derived values, but EBT and barotropic-like regions in the Southern Ocean stand out as markedly flat and smooth. This alignment suggests bathymetry to play an important role in moderating mesoscale eddy energetics. For reference, modeled and observed vertical structure categories at mooring sites are SO (surface mode, surface mode), Argb (barotropic-like, EBT), Irm (barotropic-like, EBT), and Papa (surface mode, baroclinic).

Slope and roughness are next considered a function of latitude and EOF_1 classification (Fig. 10). In this construction, the spatial patterns of vertical structure shown in Fig. 9, averaged across longitudes, confirm that EBT and barotropic-like structures (Fig. 10, green and orange lines) are found at higher latitudes where roughness and slope magnitudes are, on average, multiple factors smaller than BC and surface mode values at similar latitudes. This characterization is clearer in the Southern Hemisphere, with significant slopes found in EBT and barotropic-like regions at high northern latitudes, but here, these regions are less contiguous and comprise less ocean area.

The apparent relationship between the vertical partitioning of EKE and bathymetric slope and roughness (Fig. 11) appears where EOF_1 structures are single signed and do not decay to zero near the seafloor (Figs. 11d,e,i,j). While these regions comprise a range of slope and roughness values, they disproportionately contain regions that are flat and smooth. In other words, of the four vertical structure regimes considered, only in EBT and barotropic-like regions do we find a log–log linear relationship between the square root of the BT/BC EKE ratio and bathymetric slope and roughness, approximately following a slope of -0.25 (Figs. 11d,e,i,j). The smoothest regions of the seafloor are the most barotropic, and as both slope and roughness increase, the BT/BC EKE ratio decreases toward a value of one. That the BT/BC ratio appears to depend on both slope and roughness in these higher-latitude regions suggests both slope moderated modal interaction and bottom dissipation to have some effect on vertical structure throughout the water column, a result discussed from a theoretical perspective by LaCasce (2017).

In contrast, as arguably expected from the relationship between stratification and the baroclinic Rossby radius of

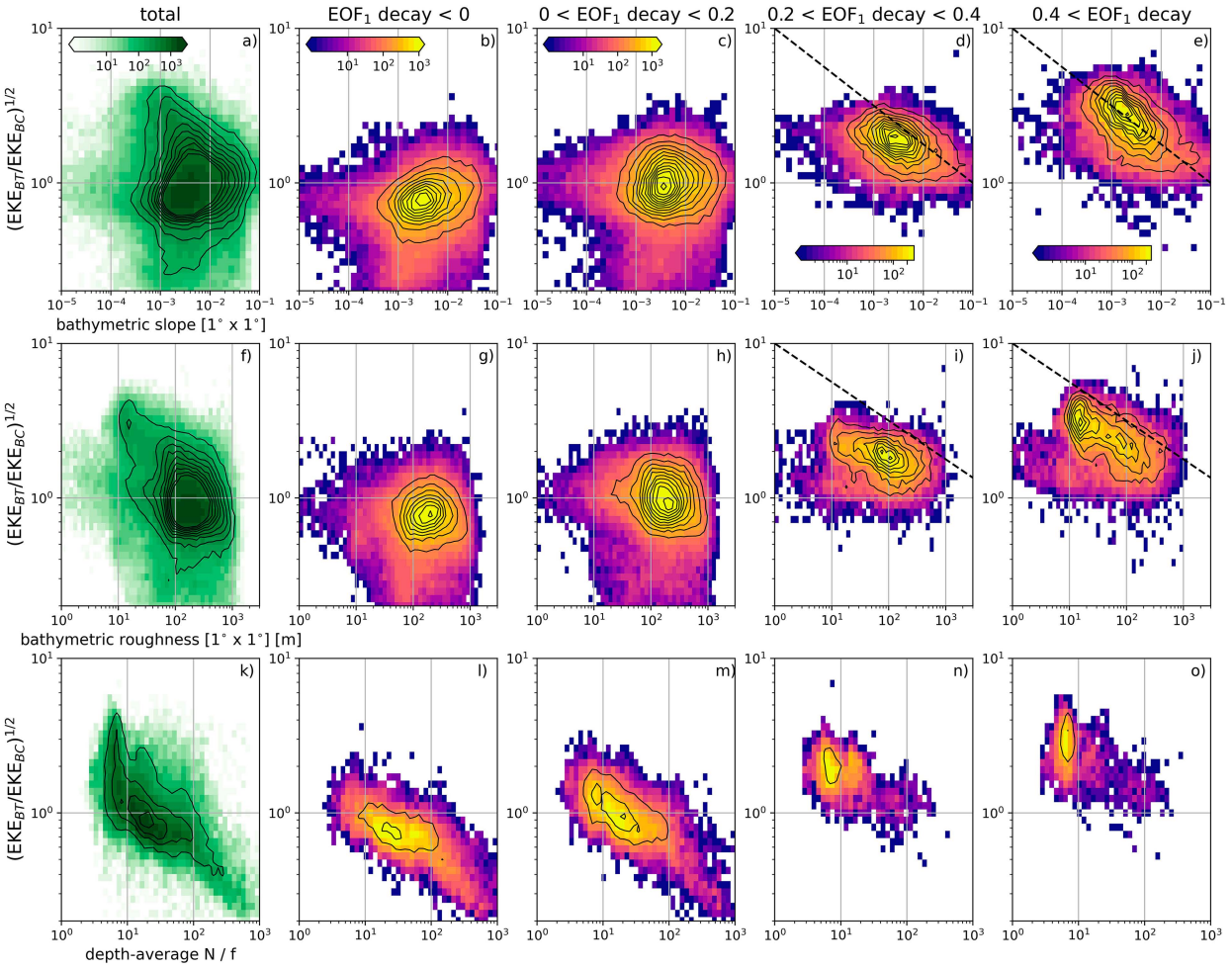

FIG. 11. (a) Global (for depths greater than 1000 m) two-dimensional histograms of bathymetric slope vs BT/BC EKE. Bins are defined in log–log space and counts (see colorbar) sum to the total number of ocean grid points. (b)–(e) As in (a), but for each of the four geographic regions defined by EOF_1 decay cutoffs. The dashed line has a slope of −0.25. (f)–(j) As in (a)–(e), but as a function of bathymetric roughness. (k)–(o) As in (a)–(e), but as a function of time-mean depth-average N/f.

deformation, we find a log–log linear relationship between BT/BC EKE and N/f (Figs. 11n,o), but only in regions where EOF_1 structures are classified as baroclinic or surface mode like. At higher latitudes, and where EOF_1 structures are single signed and do not decay to zero near the seafloor, we find no significant BT/BC EKE relationship with N/f. These results imply stratification to have a more significant role in influencing and/or moderating eddy vertical structure at lower latitudes, where eddy structures are and remain more baroclinic than at higher latitudes. At higher latitudes, and where eddy vertical structures are more barotropic, an apparent role of bathymetric slope and roughness is evident. These choices to plot slope, roughness, and stratification against the square root of the BT/BC EKE ratio represent an attempt to create an analog to the scalings derived by Gallet and Ferrari (2020, 2021) in relating eddy vertical and horizontal scales. The qualitative results are fundamentally unchanged if a different metric of vertical structure, like EOF_1 decay, is considered (not shown).

5. Discussion

In this analysis, we identify a relationship between the vertical partitioning of eddy kinetic energy and ocean bathymetry. We present a synthesis of observation- and model-based analyses, demonstrating compelling agreement between the two, that reveals where bathymetric slope and roughness moderate eddy vertical structure. In agreement with past studies (e.g., LaCasce 2017), we find vertical structure to not be primarily influenced by spatial variations in seafloor topography, but rather that stratification, latitude, mean flow, and bathymetry all play a role and contribute to a diverse landscape. The relevance of many factors is evident in observations along a continental slope at Irm, where flow is topographically steered and follows the conservation expectations of planetary vorticity (f/H). Despite the presence of a steep slope, eddy vertical structures align with flat-bottom mode expectations, a result of isobath following flow. Elsewhere, where bathymetric slopes are more moderate (e.g., the SO site), we argue that bathymetric

roughness plays a role in shaping the vertical structure of eddy kinetic energy. That a similar relationship appears between vertical structure and slope and vertical structure and roughness (Figs. 11e,j) suggests the two to play a similar role; however, more serious evaluation is needed from a geomorphological perspective that considers the diversity of combinations of slope, roughness, and eddy propagation direction relative to bathymetry orientation.

In line with expectations developed from a derivation of dynamical modes (section 3b), we find a relationship between vertical structure and depth-average N/f. At lower latitudes and where EOF_1 structures are more baroclinic, the BT/BC EKE ratio decreases as N/f increases (Figs. 11k–o). Theoretical expectation and past results demonstrate that stratification plays an important role in influencing eddy vertical structure, particularly in the decay in vertical structure amplitude with increasing depth and inverse cascade strength. Simulations from Smith and Vallis (2001) reveal that, compared to turbulent cascades in a uniformly stratified ocean, transfers of energy from baroclinic modes to the barotropic mode are relatively inhibited in the presence of upper-ocean intensified stratification. This may at least partly explain why, across all latitudes, dominant eddy vertical structures (Fig. 10b) are not barotropic and have horizontal length scales only a few times greater than local deformation radii (Klocker et al. 2016). One might only expect the limit of the inverse cascade of EKE to correspond to horizontal scales at the Rhines scale and barotropic vertical structure if the stratification were uniform and the seafloor flat. Here, we find the barotropic fraction of EKE to increase as N/f decreases (Figs. 11k–o), but only in regions characterized as baroclinic and surface mode like (Figs. 11d,e,i,j). In EBT and barotropic-like regions, N/f does not appear to scale as strongly with the BT/BC EKE ratio.

In particular, these results empirically identify a role played by bathymetry in which eddy vertical structures become more baroclinic as slope and roughness increase. Where principal EOF structures are more uniform in depth (e.g., equivalent barotropic or barotropic mode like), we find a dependence of the vertical partitioning of EKE on bathymetric slope and roughness. As slope and roughness increase, the fraction of barotropic EKE decreases. That this relationship only appears at higher latitudes suggests mid- and lower-latitude eddy structures to be moderated to a greater degree by stratification and other factors. Turbulent regime dependence on latitude is also apparent considering the scale separation between the deformation radius and Rhines scale, the length scale at which changes in the Coriolis frequency are felt. This scale separation decreases with latitude such that lower-latitude eddy characterizations align with planetary wave theory. Gallet and Ferrari (2020, 2021) characterize this dependence of eddy structure on latitude defining low-latitude zonostrophic or β-plane turbulence and high-latitude f-plane vortex gas turbulence regimes. The emergence of a relationship between vertical structure and bathymetry only at higher latitudes suggests that bathymetry exerts some control on vertical structure in this vortex gas regime, where there exists a sufficient length-scale separation between instability and planetary wave scales (Klocker et al. 2016).

These four OOI mooring locations span a reasonable range of background conditions in the global ocean and thus provide a good first approach to the assessment or validation of full-depth vertical velocity structure in global models. A range of stratification, total kinetic energy, bottom slope, and bottom roughness are captured, although particularly large stratification regimes are not represented (Fig. 2). This analysis also demonstrates that observations and models must be treated similarly for meaningful comparisons (Fig. 7) and that simple metrics (e.g., the BT/BC ratio), as opposed to dynamical modes, can be effective for comparison. Regardless of the methods used for quantifying vertical structure, the vertical structure of key variables, including stratification and kinetic energy, is important to quantify in assessing and validating numerical models.

This analysis has some implications for the ability to reconstruct interior velocities from surface velocities (e.g., Isern-Fontanet et al. 2008; Wang et al. 2013; Liu et al. 2017) and reveals dependence on the location and known hydrographic and bathymetric features. As this relates to topographic slope and roughness, our results suggest that the assumption of surface mode-like vertical structure is adequate at most, especially mid-, latitudes, with the exception of regions with elevated EKE identified as flat and smooth. At these locations, spanning roughly 20% of the global ocean area, assumptions of surface-mode structure will result in the substantial underestimation of deep eddy velocities and implied dissipation. Regions of varied eddy vertical structure may also imply spatial patterns in eddy phase speed. Barotropic-like structures should have faster speeds that are in closer alignment with satellite-observed measurements of eddy propagation speeds greater than those associated with flat-bottom modes (Tulloch et al. 2009). Bathymetry features should be investigated in future work.

The results presented here are framed to demonstrate that eddy vertical structures span the range of theoretical expectations and that care should be taken in prescribing a universal structure. Overall, flat-bottom modes (e.g., Wunsch 1997) are readily acknowledged as insufficient in their representation of eddy vertical structure but often used in a prescriptive sense due to the ease of their calculation and use. More recent analyses (e.g., de La Lama et al. 2016; LaCasce 2017; LaCasce and Groeskamp 2020) demonstrate the realism of sloping-bottom modes and their ability to represent the full range of vertical structures, including flat-bottom mode cases, but acknowledge their complicated dependence on the horizontal wavenumber relative to the bathymetric slope angle. The authors thus recommend adopting vertical structures like surface modes due to their similarity to observed structures and general utility. We show in particular that knowledge of seafloor bathymetry can be used to guide or develop expectation as to this landscape of vertical structure. We acknowledge that our assessment of the role of bathymetry considers slope and roughness only at mesoscales and excludes additional dynamical characterizations of the flow that shape vertical structure. Despite this, our results motivate the consideration of seafloor bathymetry in applications or modeling efforts that prescribe eddy vertical structure or effects. We also highlight that the consideration of bathymetry features in vertical structure analyses permits both flat-bottom and surface mode structures to be regionally expressed.

6. Conclusions

We conclude from several pieces of evidence that bathymetry influences eddy vertical structure not only near the seafloor but also throughout the water column. Specifically, as bathymetric slope and roughness increase, eddy vertical structures become more baroclinic. At the four Ocean Observatories Initiative mooring sites considered here, observed eddy vertical structures revealed similarities to both dynamical flat-bottom and sloping-bottom vertical modes, but overall, no universal vertical structure. The contrast in vertical structure especially between the Southern Ocean and Argentine Basin sites at similar latitudes strongly suggests that bathymetric slope and/or roughness are influential. Globally, the characterization of vertical structure EOFs in a high-resolution coupled atmosphere–ocean model revealed distinct regions of barotropic or baroclinic dominance, with a spatial pattern strikingly similar to that of bathymetric roughness (Fig. 8). A quantitative investigation confirmed this relationship in regions where velocity decayed minimally with depth, primarily deep basins comprising 20% of the total ocean area and predominantly located at higher latitude. In these regions, the barotropic to baroclinic eddy kinetic energy ratio decreases by a factor of 5 for an approximate doubling of slope magnitude and a fivefold increase in bathymetric roughness (Fig. 11).

These results are consistent with expectation that mesoscale turbulence cascades are moderated by bathymetry in manner expected from linear quasigeostrophic turbulence theory, like that detailed by LaCasce (2017). We additionally conclude that the four OOI mooring sites span a reasonable range of background conditions in the global ocean and thus provide one approach to the assessment or validation of full-depth vertical structure in global models. Agreement between NOAA GFDL's CM2.6 and observed vertical structure motivated the use of this simulation output to consider a relationship between bathymetry and vertical structure globally. Because eddy vertical structures influence many dynamical ocean processes, like meridional tracer and heat transport, it is important to quantify and validate eddy characteristics in numerical models. That bathymetry influences eddy vertical structure has several practical implications. These results confirm that care must be taken when inferring interior properties from more abundant surface or upper-ocean observations as there is no universal vertical structure. Bathymetric slope and roughness can be leveraged to improve such estimates. Furthermore, knowledge and characterization of bathymetric features can inform mesoscale eddy parameterization development, particularly as it relates to the mesoscale energy budget (Marshall and Naviera-Garabato 2008), such that eddy parameterizations are not only flow or scale aware (e.g., Jansen et al. 2019) but also bathymetry aware.

Acknowledgments. We would like to acknowledge and thank the entire Climate Process Team on Ocean Transport and Eddy Energy for continued and meaningful feedback as well as Wenda Zhang for his detailed feedback and recommendations. This work was generously funded by NSF Grants OCE-1912302 (Cole and Steinberg, during his time at WHOI), OCE-1912357 (Yankovsky, Zanna), and NOAA CVP NA19OAR4310364 (Zanna). We would also like to thank an anonymous reviewer and Joe LaCasce for their detailed reviews and suggestions for improvement.

Data availability statement. Mooring observations of horizontal velocity and temperature can be obtained at https://oceanobservatories.org/data-portal/ and those developed for the investigation of subinertial variability at the Woods Hole Open Access Server Uniform Resource Identifier can be obtained at https://hdl.handle.net/1912/66426 and https://doi.org/10.26025/1912/66426. Argo profiling float–derived climatologies of temperature and salinity (Roemmich and Gilson 2009) used in created time-mean density profiles can be obtained at https://sio-argo.ucsd.edu/RG_Climatology.html. Satellite altimeter–derived surface velocities can be downloaded from the Copernicus Marine Service (CMEMS 2024). NOAA GFDL CM2.6 output can be obtained at https://catalog.pangeo.io/browse/master/ocean/GFDL_CM2_6/.

REFERENCES

Beckmann, A., 1988: Vertical structure of midlatitude mesoscale instabilities. *J. Phys. Oceanogr.*, **18**, 1354–1371, https://doi.org/10.1175/1520-0485(1988)018<1354:VSOMMI>2.0.CO;2.

Brink, K. H., and J. Pedlosky, 2020: The structure of baroclinic modes in the presence of baroclinic mean flow. *J. Phys. Oceanogr.*, **50**, 239–253, https://doi.org/10.1175/JPO-D-19-0123.1.

Charney, J., 1971: Geostrophic turbulence. *J. Atmos. Sci.*, **28**, 1087–1095, https://doi.org/10.1175/1520-0469(1971)028<1087:GT>2.0.CO;2.

Chelton, D. B., M. G. Schlax, and R. M. Samelson, 2011: Global observations of nonlinear mesoscale eddies. *Prog. Oceanogr.*, **91**, 167–216, https://doi.org/10.1016/j.pocean.2011.01.002.

CMEMS, 2024: Global ocean gridded L 4 sea surface heights and derived variables reprocessed Copernicus Climate Service. E.U. Copernicus Marine Service Information, Marine Data Store, accessed 24 May 2021, https://doi.org/10.48670/moi-00145.

Cowles, T., J. Delaney, J. Orcutt, and R. Weller, 2010: The ocean observatories initiative: Sustained ocean observing across a range of spatial scales. *Mar. Technol. Soc. J.*, **44**, 54–64, https://doi.org/10.4031/MTSJ.44.6.21.

de La Lama, M. S., J. H. LaCasce, and H. K. Fuhr, 2016: The vertical structure of ocean eddies. *Dyn. Stat. Climate Syst.*, **1**, dzw001, https://doi.org/10.1093/climsys/dzw001.

Delworth, T. L., and Coauthors, 2006: GFDL's CM2 global coupled climate models. Part I: Formulation and simulation characteristics. *J. Climate*, **19**, 643–674, https://doi.org/10.1175/JCLI3629.1.

——, and Coauthors, 2012: Simulated climate and climate change in the GFDL CM2.5 high-resolution coupled climate model. *J. Climate*, **25**, 2755–2781, https://doi.org/10.1175/JCLI-D-11-00316.1.

Fox-Kemper, B., and Coauthors, 2019: Challenges and prospects in ocean circulation models. *Front. Mar. Sci.*, **6**, 65, https://doi.org/10.3389/fmars.2019.00065.

Fu, L.-L., and G. R. Flierl, 1980: Nonlinear energy and enstrophy transfers in a realistically stratified ocean. *Dyn. Atmos. Oceans*, **4**, 219–246, https://doi.org/10.1016/0377-0265(80)90029-9.

Gallet, B., and R. Ferrari, 2020: The vortex gas scaling regime of baroclinic turbulence. *Proc. Natl. Acad. Sci. USA*, **117**, 4491–4497, https://doi.org/10.1073/pnas.1916272117.

——, and ——, 2021: A quantitative scaling theory for meridional heat transport in planetary atmospheres and oceans. *AGU Adv.*, **2**, e2020AV000362, https://doi.org/10.1029/2020AV000362.

Gill, A. E., J. S. A. Green, and A. J. Simmons, 1974: Energy partition in the large-scale ocean circulation and the production of mid-ocean eddies. *Deep-Sea Res. Oceanogr. Abstr.*, **21**, 499–528, https://doi.org/10.1016/0011-7471(74)90010-2.

Gnanadesikan, A., and Coauthors, 2006: GFDL's CM2 global coupled climate models. Part II: The baseline ocean simulation. *J. Climate*, **19**, 675–697, https://doi.org/10.1175/JCLI3630.1.

Griffies, S. M., 2012: Elements of the Modular Ocean Model (MOM): 2012 release with updates. NOAA/Geophysical Fluid Dynamics Laboratory, GFDL Ocean Group Tech. Rep. 7, 645 pp., https://mom-ocean.github.io/assets/pdfs/MOM5_manual.pdf.

——, and Coauthors, 2005: Formulation of an ocean model for global climate simulations. *Ocean Sci.*, **1**, 45–79, https://doi.org/10.5194/os-1-45-2005.

——, and Coauthors, 2015: Impacts on ocean heat from transient mesoscale eddies in a hierarchy of climate models. *J. Climate*, **28**, 952–977, https://doi.org/10.1175/JCLI-D-14-00353.1.

Groeskamp, S., J. H. LaCasce, T. J. McDougall, and M. Roge, 2020: Full-depth global estimates of ocean mesoscale eddy mixing from observations and theory. *Geophys. Res. Lett.*, **47**, e2020GL089425, https://doi.org/10.1029/2020GL089425.

Hallberg, R., 2013: Using a resolution function to regulate parameterizations of oceanic mesoscale eddy effects. *Ocean Model.*, **72**, 92–103, https://doi.org/10.1016/j.ocemod.2013.08.007.

Harrison, C. S., M. C. Long, N. S. Lovenduski, and J. K. Moore, 2018: Mesoscale effects on carbon export: A global perspective. *Global Biogeochem. Cycles*, **32**, 680–703, https://doi.org/10.1002/2017GB005751.

Held, I. M., and V. D. Larichev, 1996: A scaling theory for horizontally homogeneous, baroclinically unstable flow on a beta plane. *J. Atmos. Sci.*, **53**, 946–952, https://doi.org/10.1175/1520-0469(1996)053<0946:ASTFHH>2.0.CO;2.

Hua, B. L., and D. B. Haidvogel, 1986: Numerical simulations of the vertical structure of quasi-geostrophic turbulence. *J. Atmos. Sci.*, **43**, 2923–2936, https://doi.org/10.1175/1520-0469(1986)043<2923:NSOTVS>2.0.CO;2.

Isern-Fontanet, J., G. Lapeyre, P. Klein, B. Chapron, and M. W. Hecht, 2008: Three-dimensional reconstruction of oceanic mesoscale currents from surface information. *J. Geophys. Res.*, **113**, C09005, https://doi.org/10.1029/2007JC004692.

Jansen, M. F., A. Adcroft, S. Khani, and H. Kong, 2019: Toward an energetically consistent, resolution aware parameterization of ocean mesoscale eddies. *J. Adv. Model. Earth Syst.*, **11**, 2844–2860, https://doi.org/10.1029/2019MS001750.

Jing, Z., and Coauthors, 2020: Maintenance of mid-latitude oceanic fronts by mesoscale eddies. *Sci. Adv.*, **6**, eaba7880, https://doi.org/10.1126/sciadv.aba7880.

Kamenkovich, I., Z. Garraffo, R. Pennel, and R. A. Fine, 2017: Importance of mesoscale eddies and mean circulation in ventilation of the Southern Ocean. *J. Geophys. Res. Oceans*, **122**, 2724–2741, https://doi.org/10.1002/2016JC012292.

Killworth, P. D., D. B. Chelton, and R. A. de Szoeke, 1997: The speed of observed and theoretical long extratropical planetary waves. *J. Phys. Oceanogr.*, **27**, 1946–1966, https://doi.org/10.1175/1520-0485(1997)027<1946:TSOOAT>2.0.CO;2.

Klocker, A., D. P. Marshall, S. R. Keating, and P. L. Read, 2016: A regime diagram for ocean geostrophic turbulence. *Quart. J. Roy. Meteor. Soc.*, **142**, 2411–2417, https://doi.org/10.1002/qj.2833.

LaCasce, J. H., 2017: The prevalence of oceanic surface modes. *Geophys. Res. Lett.*, **44**, 11 097–11 105, https://doi.org/10.1002/2017GL075430.

——, and A. Mahadevan, 2006: Estimating subsurface horizontal and vertical velocities from sea-surface temperature. *J. Mar. Res.*, **64**, 695–721, https://doi.org/10.1357/002224006779367267.

——, and J. Wang, 2015: Estimating subsurface velocities from surface fields with idealized stratification. *J. Phys. Oceanogr.*, **45**, 2424–2435, https://doi.org/10.1175/JPO-D-14-0206.1.

——, and S. Groeskamp, 2020: Baroclinic modes over rough bathymetry and the surface deformation radius. *J. Phys. Oceanogr.*, **50**, 2835–2847, https://doi.org/10.1175/JPO-D-20-0055.1.

Lapeyre, G., and P. Klein, 2006: Dynamics of the upper oceanic layers in terms of surface quasigeostrophy theory. *J. Phys. Oceanogr.*, **36**, 165–176, https://doi.org/10.1175/JPO2840.1.

Larichev, V. D., and I. M. Held, 1995: Eddy amplitudes and fluxes in a homogeneous model of fully developed baroclinic instability. *J. Phys. Oceanogr.*, **25**, 2285–2297, https://doi.org/10.1175/1520-0485(1995)025<2285:EAAFIA>2.0.CO;2.

Li, G., L. Cheng, J. Zhu, K. E. Trenberth, M. E. Mann, and J. P. Abraham, 2020: Increasing ocean stratification over the past half-century. *Nat. Climate Change*, **10**, 1116–1123, https://doi.org/10.1038/s41558-020-00918-2.

Liu, L., S. Peng, and R. X. Huang, 2017: Reconstruction of ocean's interior from observed sea surface information. *J. Geophys. Res. Oceans*, **122**, 1042–1056, https://doi.org/10.1002/2016JC011927.

Mahadevan, A., E. D'Asaro, C. Lee, and M. J. Perry, 2012: Eddy-driven stratification initiates North Atlantic spring phytoplankton blooms. *Science*, **337**, 54–58, https://doi.org/10.1126/science.1218740.

Marshall, D. P., and A. C. Naviera-Garabato, 2008: A conjecture on the role of bottom-enhanced diapycnal mixing in the parameterization of geostrophic eddies. *J. Phys. Oceanogr.*, **38**, 1607–1613, https://doi.org/10.1175/2007JPO3619.1.

McCoy, D., D. Bianchi, and A. L. Stewart, 2020: Global observations of submesoscale coherent vortices in the ocean. *Prog. Oceanogr.*, **189**, 102452, https://doi.org/10.1016/j.pocean.2020.102452.

MODE-Group, 1978: The mid-ocean dynamics experiment. *Deep-Sea Res.*, **25**, 859–910, https://doi.org/10.1016/0146-6291(78)90632-X.

Patel, R. S., J. Llort, P. G. Strutton, H. E. Phillips, S. Moreau, P. C. Pardo, and A. Lenton, 2020: The biogeochemical structure of Southern Ocean mesoscale eddies. *J. Geophys. Res. Oceans*, **125**, e2020JC016115, https://doi.org/10.1029/2020JC016115.

Pelland, N. A., C. C. Eriksen, and M. F. Cronin, 2016: Seaglider surveys at Ocean Station Papa: Circulation and water mass properties in a meander of the North Pacific Current. *J. Geophys. Res. Oceans*, **121**, 6816–6846, https://doi.org/10.1002/2016JC011920.

Rhines, P. B., 1979: Geostrophic turbulence. *Annu. Rev. Fluid Mech.*, **11**, 401–441, https://doi.org/10.1146/annurev.fl.11.010179.002153.

Rocha, C. B., I. C. A. da Silveira, B. M. Castro, and J. A. M. Lima, 2014: Vertical structure, energetics, and dynamics of the Brazil Current System at 22°S–28°S. *J. Geophys. Res. Oceans*, **119**, 52–69, https://doi.org/10.1002/2013JC009143.

Roemmich, D., and J. Gilson, 2009: The 2004–2008 mean and annual cycle of temperature, salinity, and steric height in the global ocean from the Argo Program. *Prog. Oceanogr.*, **82**, 81–100, https://doi.org/10.1016/j.pocean.2009.03.004.

Siegelman, L., P. Klein, P. Rivière, A. F. Thompson, H. S. Torres, M. Flexas, and D. Menemenlis, 2020: Enhanced upward heat transport at deep submesoscale ocean fronts. *Nat. Geosci.*, **13**, 50–55, https://doi.org/10.1038/s41561-019-0489-1.

Smith, K. S., 2007: The geography of linear baroclinic instability in Earth's oceans. *J. Mar. Res.*, **65**, 655–683, https://doi.org/10.1357/002224007783649484.

Smith, S., and G. Vallis, 2001: The scales and equilibration of midocean eddies: Freely evolving flow. *J. Phys. Oceanogr.*, **31**, 554–571, https://doi.org/10.1175/1520-0485(2001)031<0554:TSAEOM>2.0.CO;2.

Smith, W. H. F., and D. T. Sandwell, 1997: Global sea floor topography from satellite altimetry and ship depth soundings. *Science*, **277**, 1956–1962, https://doi.org/10.1126/science.277.5334.1956.

Steinberg, J. M., and C. C. Eriksen, 2022: Eddy vertical structure and variability: Deepglider observations in the North Atlantic. *J. Phys. Oceanogr.*, **52**, 1091–1110, https://doi.org/10.1175/JPO-D-21-0068.1.

Toole, J. M., R. C. Musgrave, E. C. Fine, J. M. Steinberg, and R. A. Krishfield, 2023: On the vertical structure of deep-ocean subinertial variability. *J. Phys. Oceanogr.*, **53**, 2913–2932, https://doi.org/10.1175/JPO-D-23-0011.1.

Tulloch, R., J. Marshall, and K. S. Smith, 2009: Interpretation of the propagation of surface altimetric observations in terms of planetary waves and geostrophic turbulence. *J. Geophys. Res.*, **114**, C02005, https://doi.org/10.1029/2008JC005055.

Wang, D.-P., C. N. Flagg, K. Donohue, and H. T. Rossby, 2010: Wavenumber spectrum in the Gulf Stream from shipboard ADCP observations and comparison with altimetry measurements. *J. Phys. Oceanogr.*, **40**, 840–844, https://doi.org/10.1175/2009JPO4330.1.

Wang, J., G. R. Flierl, J. H. LaCasce, J. L. McClean, and A. Mahadevan, 2013: Reconstructing the ocean's interior from surface data. *J. Phys. Oceanogr.*, **43**, 1611–1626, https://doi.org/10.1175/JPO-D-12-0204.1.

Wunsch, C., 1997: The vertical partition of oceanic horizontal kinetic energy. *J. Phys. Oceanogr.*, **27**, 1770–1794, https://doi.org/10.1175/1520-0485(1997)027<1770:TVPOOH>2.0.CO;2.

——, and D. Stammer, 1997: Atmospheric loading and the oceanic "inverted barometer" effect. *Rev. Geophys.*, **35**, 79–107, https://doi.org/10.1029/96RG03037.

——, and R. Ferrari, 2004: Vertical mixing, energy, and the general circulation of the oceans. *Annu. Rev. Fluid Mech.*, **36**, 281–314, https://doi.org/10.1146/annurev.fluid.36.050802.122121.

Xu, Y., and L.-L. Fu, 2011: Global variability of the wavenumber spectrum of oceanic mesoscale turbulence. *J. Phys. Oceanogr.*, **41**, 802–809, https://doi.org/10.1175/2010JPO4558.1.

Yankovsky, E., L. Zanna, and K. S. Smith, 2022: Influences of mesoscale ocean eddies on flow vertical structure in a resolution-based model hierarchy. *J. Adv. Model. Earth Syst.*, **14**, e2022MS003203, https://doi.org/10.1029/2022MS003203.

——, S. Bachman, K. S. Smith, and L. Zanna, 2024: Vertical structure and energetic constraints for a backscatter parameterization of ocean mesoscale eddies. *J. Adv. Model. Earth Syst.*, **16**, e2023MS004093, https://doi.org/10.1029/2023MS004093.

Zanna, L., and Coauthors, 2019: Climate process team: Ocean transport and eddy energy. NSF NOAA Proposal, 22 pp., https://doi.org/10.6084/m9.figshare.10105922.v1.

Zhang, L., and T. L. Delworth, 2015: Analysis of the characteristics and mechanisms of the Pacific decadal oscillation in a suite of coupled models from the geophysical fluid dynamics laboratory. *J. Climate*, **28**, 7678–7701, https://doi.org/10.1175/JCLI-D-14-00647.1.

Zhang, W., S. M. Griffies, R. W. Hallberg, Y.-H. Kuo, and C. L. P. Wolfe, 2024: The role of surface potential vorticity in the vertical structure of mesoscale eddies in wind-driven ocean circulations. *J. Phys. Oceanogr.*, **54**, 1243–1266, https://doi.org/10.1175/JPO-D-23-0203.1.

Zhao, J., A. Bower, J. Yang, X. Lin, and N. P. Holliday, 2018a: Meridional heat transport variability induced by mesoscale processes in the subpolar North Atlantic. *Nat. Commun.*, **9**, 1124, https://doi.org/10.1038/s41467-018-03134-x.

Zhao, M., M.-L. Timmermans, R. Krishfield, and G. Manucharyan, 2018b: Partitioning of kinetic energy in the Arctic Ocean's Beaufort Gyre. *J. Geophys. Res. Oceans*, **123**, 4806–4819, https://doi.org/10.1029/2018JC014037.

Zou, S., A. S. Bower, H. Furey, R. S. Pickart, L. Houpert, and N. Holliday, 2021: Observed deep cyclonic eddies around Southern Greenland. *J. Phys. Oceanogr.*, **51**, 3235–3252, https://doi.org/10.1175/JPO-D-20-0288.1.